Article

Suppressing ROS Production of AIE Nanoprobes by Simple Matrices Optimization for CNS Cell Observation and Minimized Influence of Cytoskeleton Morphology

Xiaotong Chen, Yajing Jiang, Jiaxin Liu, Yu Tian, Yifan Deng, Xiaoqiong Li,* Wenbo Wu,* Ruoyu Zhang,* and Yulin Deng*

Cite This: Chem. Biomed. Imaging 2024, 2, 775–783

Read Online

ACCESS | Metrics & More | Article Recommendations | Supporting Information

ABSTRACT: The visualization of the central nervous system (CNS) has proposed stringent criteria for fluorescent probes, as the inevitable production of reactive oxygen species (ROS) or heat generated from most photoluminescent probes upon excitation can disturb the normal status of relatively delicate CNS cells. In this work, a red-emitting fluorogen with aggregation-induced emission (AIE) characteristics, known as DTF, was chosen as the model fluorogen to investigate whether the side effects of ROS and heat could be suppressed through easy-to-operate processes. Specifically, DTF was encapsulated with different amphiphilic matrices to yield AIE nanoprobes, and their photoluminescent properties, ROS production, and photothermal conversion rates were examined. BSA@DTF NPs possessed 1.3-fold brightness compared to that of DSPE-PEG@DTF NPs and F127@ DTF NPs but its ROS generation efficiency is markedly decreased to only 2.4% of that produced by F127@DTF NPs. Meanwhile, BSA@DTF NPs showed a negligible photothermal effect. These features make BSA@DTF NPs favorable for long-term live cell imaging, particularly for fluorescent imaging of CNS cells. BSA@DTF NPs were able to sustain the normal state of HT-22 neuronal cells with continuous illumination for at least 25 min, and they also preserved the cytoskeleton of microglia BV-2 cells as the untreated control group. This work represents a successful but easy-to-operate process to suppress the ROS generation of red-emissive AIEgen, and it highlights the importance of minimizing the ROS generation of the fluorescent probes, particularly in the application of long-term imaging of CNS cells.

KEYWORDS: matrices optimization, suppressing ROS, cytoskeleton morphology, neuron cell imaging, microglia
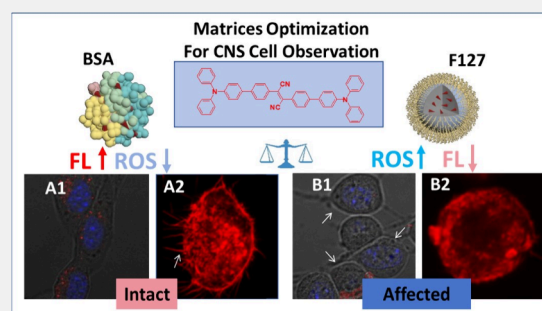
■ INTRODUCTION

Increasing research attentions in the fields of brain research have made it urgent to develop suitable imaging tools to facilitate the physiological and pathological investigation in central nervous system (CNS).[1−3] Fluorescent probes are one of the important candidates due to their good sensitivity, ease of modification, and good selectivity/targeting ability.[4−7] Traditional fluorogens suffer from detrimental aggregation-caused quenching (ACQ), which can be effectively overcome by fluorogens with aggregation-induced emission (AIE) characteristics. In addition, expanding the emission window of fluorescent dyes to longer wavelength is always desirable because they enjoy better tissue penetration and fewer overlaps with the short-wavelength autofluorescence in biological environment.[8] Modulation of chemical structures has been proved useful in developing red-emissive fluorogens, commonly used strategies including elongating conjugation, increasing the rigidity of chemical structure, and inserting D−A structures (Scheme 1).[9,10] For propeller-shaped AIEgen, modulation of the D−A or D−A−D structures is a more

commonly used way to produce red-emissive fluorogens,[11−13] however, the existence of D−A pairs inevitably splits up the HOMO and LOMO distribution, which further decreases ΔE_{ST} and promotes the ROS production.[14,15] Though ROS production and photothermal conversion are valuable in ablation of cancer cells.[16,17] Unfortunately, excessive ROS is harmful for normal cells and tissues. Furthermore, it may also trigger inflammation and take part in the pathogenesis and development of neurological disorder.[18−20] In this regard, red-emissive AIEgens with little ROS generation are extremely useful tools for live cell imaging of CNS cells.

Another prerequisite of applying fluorescent dyes to imaging is to endow their good solubility or good dispersity in an

Scheme 1. Modulation of Fluorescent Brightness and ROS Generation by Different Post-Synthesis Encapsulation Using Matrices Including BSA, DSPE-PEG$_{2000}$, and F127
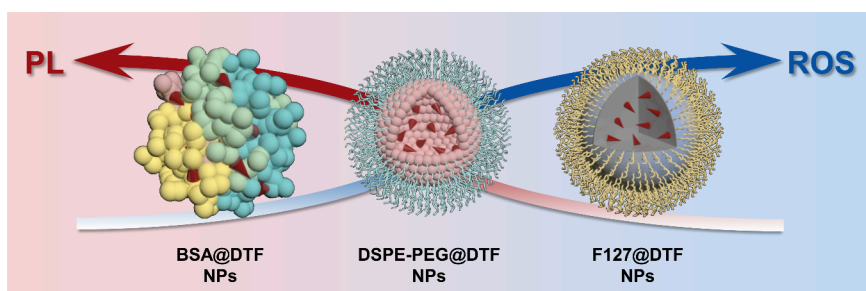
aqueous medium. Organic fluorogens are commonly hydrophobic, but encapsulation into nanoparticles could endow them with good solubility, water-dispersibility, and the possibility for further surface modifications. Well-established encapsulation scaffolds for fluorescent bioimaging include silica NPs, liposomes NPs, polymeric NPs (Pluronic F127, PLGA, PEG), etc.[21−24] In addition, serum albumin, a good matrix for drug carriers, has also attracted increasing research attention. The hydrophobic pockets of serum albumin could confine fluorescent dyes to take a rigid conformation, which help to minimize the torsional rotations and avoid radiative decays, particularly for molecules with propeller structures.[25]

In this work, an AIEgen DTF was selected as the model compound. DTF was encapsulated by different matrices, including bovine serum albumin (BSA), DSPE-PEG$_{2000}$, and F127, yielding BSA@DTF NPs, DSPE-PEG@DTF NPs, and F127@DTF NPs, respectively. Their photoluminescence, ROS generation ability, and photothermal conversion efficiency were determined and compared. Subsequently, to explore the usefulness of BSA@DTF NPs for the live cell imaging, cellular uptake, intracellular ROS generation, and long-term fluorescent imaging under continuous laser illumination were studied and compared with other nanoprobes by coincubation with neuronal cell HT-22. In addition, the three nanoprobes were incubated with murine microglia cell BV-2, and their cytoskeleton morphology was observed since the cytoskeleton plays vital roles in cellular activities. The results showed that only BSA@DTF NPs could maintain the cytoskeleton of BV-2 cells as the control group without any treatment.

■ EXPERIMENTAL SECTION

General Information

The solvents and reagents, instrumental information, and cellular experiments were presented in Supporting Information (SI).

Synthesis of DTF

According to the previous report, DTF (2,3-bis(4′-(diphenylamino)-[1,1′-biphenyl]-4-yl) fumaronitrile) was synthesized through a Suzuki coupling reaction between phenylboronic acid and 2,3-bis(4-bromophenyl)-2-butenedinitrile in the presence of tetrakis-(triphenylphosphine)palladium as catalysis and a base potassium carbonate to get product as a dark red solid with the yield of 80%. The structure was confirmed by mass spectrometry and NMR spectroscopy.

Preparation of BSA@DTF NPs, DSPE-PEG@DTF NPs, and F127@DTF NPs

All the NPs were prepared according to previous reports.[22,26,27] Specifically, DTF was first dissolved in THF and mixed with matrices including BSA, DSPE-PEG$_{2000}$, and F127 in THF. Then the mixture was dispersed in PBS buffer with the assistance of ultrasonication,

followed by dialysis in deionized water for 24 h and change water every 4 h. After concentrating by ultrafiltration centrifuge tube (Millipore), nanoprobes including BSA@DTF NPs, DSPE-PEG@DTF NPs, and F127@DTF NPs were obtained and stored at 4 °C ready for use.

Measurement of UV−vis and PL Spectra of DTF and Nanoprobes

DTF was dissolved in DMF with a concentration of 10 mM, as a stock solution. The PL spectra of DTF and different DTF nanoparticles in PBS buffer were measured at the same concentration of 10 μM. The concentrations of different samples, including fluorescent NPs, were calibrated based on the UV−vis absorbance maximum of DTF, followed by collection of their PL spectra on a fluorescence spectrometer.

Assessment of ROS Generation Ability and $^1O_2$ Generation Ability

DCFH solution (40 μM) in PBS buffer was freshly prepared by hydrolyzing from DCFH-DA. Then stock solutions of BSA@DTF NPs, DSPE-PEG@DTF NPs, and F127@DTF NPs were resuspended in the solution of DCFH, respectively, to a final concentration of 1 μM according to the DTF content. The ROS generation ability of different NPs was subsequently assessed by collecting the fluorescence spectra from 495 to 650 nm, every 5 s after white light irradiation with a power density of 30 mW/cm^2. (DCFH was excited at 480 nm.) The $^1O_2$ production was detected by 9′,10′-anthracenediyl-bis-(methylene)-dimalonic acid (ABDA). Specifically, to a PBS solution of ABDA (50 μM), stock solutions of BSA@DTF NPs, DSPE-PEG@DTF NPs, and F127@DTF NPs were added, respectively, to get a final concentration of 1 μM nanoprobes according to the DTF content. The absorption spectra were monitored in a range of 330−420 nm after white light irradiation of 30 mW/cm^2 every 30 s. The absorptance decline relative to the initial value at 378 nm ($Ln(A_0/A)$) was recorded and plotted after taking the natural logarithm, to get the $^1O_2$ generation rate.

Assessment of Photothermal Properties of the Nanoprobes

The nanoprobes at the same concentration of 1 or 15 μM were subjected to white light with an intensity of 30, 45, or 60 mW cm^{-2} for 8 min. During this process, the temperature was continuously monitored and the irradiation was halted once the temperature approached a stable plateau. Additionally, a control experiment utilizing pure water under identical conditions was concurrently conducted for comparative purposes.

Evaluation of Cell Viability by CCK-8 kit

The cytotoxicity of the nanoprobes were assessed by coincubation with HT-22 cells followed by measurement of cell viability using Cell Counting Kit-8 (CCK-8) assays. HT-22 cells were seeded in 96-well plates (5×10^3 cells/well) and incubated to allow cells adhere to the plates. After 12 h of incubation with nanoprobes including BSA@DTF NPs, DSPE-PEG@DTF NPs, and F127@DTF NPs, respectively, HT-22 cells in each well were washed with PBS after removal of nanoprobes in culture medium. Subsequently, 10 μL of CCK-8
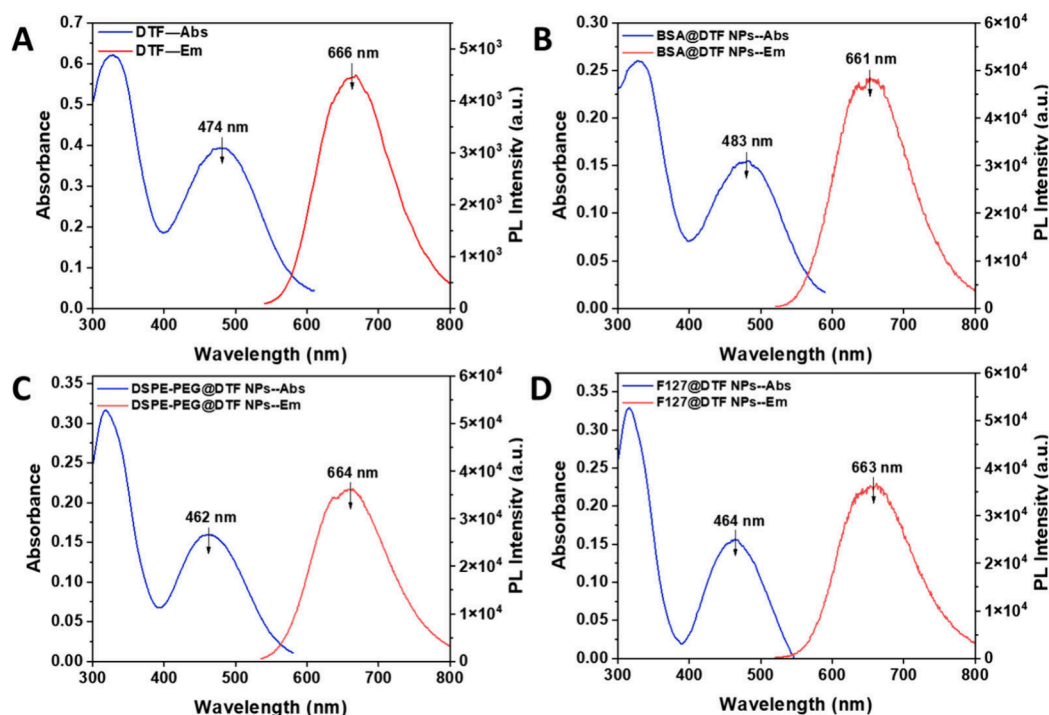
Figure 1. UV−vis absorption and photoluminescence spectra of (A) DTF, (B) BSA@DTF NPs, (C) DSPE-PEG@DTF NPs, and (D) F127@DTF NPs. Spectra of nanoprobes (B, C, D) were measured in PBS buffer at the same concentration of 10 μM (according to the molar concentration of DTF). Spectra of DTF was measured in the mixture of THF:PBS = 1:99 (v/v).

reagent in 100 μL of DMEM medium was added into each well and cultured for another 1 h, followed by measurement of the absorbance of the CCK-8 reagent at 450 nm by a BioTek Cytation 3 reader. The cell viability was calculated by viability (%): $(A_s/A_c) \times 100\%$ (A_s: the absorbance of sample well; A_c: the absorbance of control well).

Assessment of Cellular Uptake Behavior and Intracellular ROS Generation

Cellular uptake behavior and intracellular ROS generation of BSA@DTF NPs, DSPE-PEG@DTF NPs, and F127@DTF NPs by HT-22 cells were assessed by confocal laser scanning microscopy (CLSM). HT-22 cells were cultured in a 20 mm glass bottom confocal Petri dish at 37 °C with 5% CO$_2$ atmosphere. After cells reached 70% confluence, stock solutions of BSA@DTF NPs, DSPE-PEG@DTF NPs, and F127@DTF NPs were resuspended in the FBS-free DMEM medium to a final concentration of 15 μM, and cultured with HT-22 cells. At different incubation time points of 30 min, 1, 2, 4, 6, 8, and 12 h, cells were washed with PBS and stained with Hoechst 33342 (0.5 μL, 10 mg/mL) after the fixation with 4% PFA Fix Solution for 15 min. The fluorescence images of HT-22 cells were acquired using CLSM. Nanoprobes was excited at 488 nm and the emission was collected at 630−690 nm. Hoechst 33342 was excited at 405 nm and the emission was collected at 400−490 nm.

DCFH-DA was utilized to indicate nonspecific ROS generation inside HT-22 cells. BSA@DTF NPs, DSPE-PEG@DTF NPs, and F127@DTF NPs (15 μM according to DTF) were incubated with HT-22 cells for 12 h in the dark, respectively. Then the cells were washed and incubated with DCFH-DA (10 μMm) for 30 min, followed by removal of the probe by washing the cells with PBS buffer. The CLSM images of HT-22 cells with or without white light irradiation (30 mW/cm^2, 3 min) were collected (excitation at 488 nm, emission wavelength from 500 to 550 nm).

Fluorescent Imaging of HT-22 Cells under Continuous Laser Illumination

HT-22 cells were preincubated with BSA@DTF NPs, DSPE-PEG@DTF NPs, and F127@DTF NPs for 24 h, followed by exposure to a continuous irradiation by a 488 nm laser light equipped on the confocal microscope. Then the live cell images were taken by CLSM

every 5 min, up to 25 min. Hoechst 33342 (0.5 μL, 10 mg/mL) was employed to localize the cell nuclei with a 15 min incubation time. N anoprobes were excited at 488 nm, and the emission signals were collected from 630 to 690 nm. Hoechst 33342 was excited at 405 nm, and the emission was collected from 400 to 490 nm.

Effects of NPs on the Cytoskeleton Morphology of BV-2 Cell

BV-2 cells were cultured with BSA@DTF NPs, DSPE-PEG@DTF NPs, and F127@DTF NPs at the same concentration of 10 μM for 24 h. BV-2 cells were also treated with LPS at the concentrations of 1 and 10 μg/mL, respectively. Specifically, BV-2 cells were starved in FBS-free DMEM for 24 h after adhering to the confocal peri dish, followed by addition of LPS at the desired concentration for another 24 h. After being washed by PBS buffer, the cells were fixed with 4% PFA Fix Solution for 15 min, and their actin filament was stained by a commercial actin probe ActinRed 555 ReadyProbes Reagent (Thermo Fisher Scientific Inc., U.S.A.). ActinRed 555 ReadyProbes was excited at 561 nm, and the emission was collected from 570 to 620 nm.

■ RESULTS AND DISCUSSION

Synthesis of DTF and Preparation of BSA@DTF NPs, DSPE-PEG@DTF NPs, and F127@DTF NPs

The DTF was synthesized through a typical Suzuki coupling reaction according to previous reports.[28,29] The chemical structure was verified by ^{1}H NMR and HRMS, as shown in the SI (Figure S1 and S2). A commonly used nanoprecipitation method was employed to encapsulate DTF into biocompatible matrices, including BSA, DSPE-PEG$_{2000}$, and F127 to yield nanoprobes, including BSA@DTF NPs, DSPE-PEG@DTF NPs, and F127@DTF NPs, respectively. Generally, DTF was dissolved and mixed with the matrices in benign solvent such as THF, followed by dispersion into PBS buffer under ultrasonication. The nanoprobes are ready to use after being stirred overnight and dialyzed in deionized water. All of the
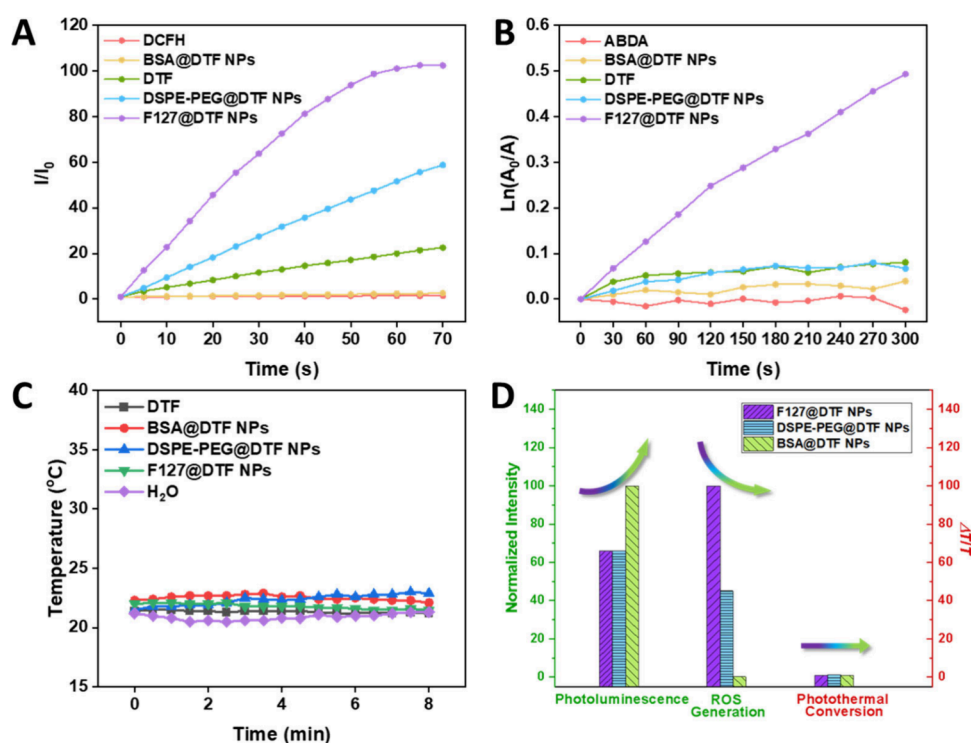
Figure 2. (A) Plots of nonspecific ROS production in the presence of DTF, BSA@DTF NPs, DSPE-PEG@DTF NPs, and F127@DTF NPs indicated by the fluorescence intensity of DCFH at 525 nm. PL intensity (I) was recorded every 5 s during white light illumination for 70 s. (B) Plots of $^1O_2$ generation of DTF, BSA@DTF NPs, DSPE-PEG@DTF NPs, and F127@DTF NPs in PBS buffers indicated by the absorbance of ABDA at 378 nm. The absorbance of ABDA was recorded under white light illumination every 30 s within 300 s. (C) Photothermal conversion efficiency of DTF, BSA@DTF NPs, DSPE-PEG@DTF NPs, and F127@DTF NPs solutions at the same concentration of 15 μM demonstrated by the temperature changes exposed to white light illumination for 8 min. The power density of white light is 60 mW/cm^2. (D) Comparison of the normalized photoluminescence ($I/I_{max} \times 100\%$, I represents the photoluminescence intensity of nanoprobes) and ROS generation ($I/I_{max} \times 100\%$, I represents the photoluminescence intensity of DCFH solution incubated with DTF and different nanoprobes), and the temperature changes ($\Delta T/T$) after 8 min white light illumination on the three types of nanoprobes as labeled.

three nanoprobes have good water-dispersity and their hydrodynamic diameters were determined to be 154 ± 4.1, 124 ± 2.6, and 57.9 ± 1.4 nm by DLS, as shown in Figure S3. TEM was further employed to observe the morphology of the nanoprobes, and the results were presented in the insets of Figure S3. The zeta potential of BSA@DTF NPs, DSPE-PEG@DTF NPs, and F127@DTF were measured to be −21.0, −30.7, and −2.2 mV, respectively. The stability of different nanoprobes was assessed by measuring their size distribution and UV–vis absorbance spectra every 2 days. As shown in Figure S4A–C, all of the nanoprobes have constant size and PDI for at least 10 days. In addition, the DTF inside all of the nanoprobes did not shown obvious decomposition within 12 days of observation, as shown in Figure S4D. The photostability of the nanoprobes was evaluated by measurement of their UV–vis absorbance at their maximum absorption wavelength every 3 min within 30 min after exposure to white light illumination, as shown in Figure S5.

Photoluminescence, Photodynamic Production, and Photothermal Conversion

The UV–vis and photoluminescence spectra of the three nanoprobes were subsequently recorded in PBS buffer at the same concentration of 10 μM (Figure 1). Obviously, BSA@DTF NPs demonstrated more red-shifted absorption peaks than the other two nanoprobes and DTF molecules. Theoretically, with the same donor and receptor, red-shifted absorption indicates better conjugation, which is beneficial to

increasing the brightness. It is in accordance with the phenomenon that BSA@DTF NPs showed the brightest fluorescent emission, around 1.3-fold that of DSPE-PEG@DTF NPs and F127@DTF NPs, with the same concentration of DTF inside nanoparticles.

Alternatively, better conjugation between donor and acceptor could inhibit the HOMO−LUMO separation, and consequently decrease the ROS production.[30] To verify this point, the photosensitization effect of the three nanoprobes was studied with the assistance of useful indicators including dichlorofluorescin (DCFH) and 9,10-anthracenediyl-bis-(methylene)dimalonic acid (ABDA) since ROS have too short lifetimes to be quantified directly.[31−33] DCFH is a useful indicator for assessing nonspecific ROS level, while ABDA was utilized to evaluate the production of singlet oxygen ($^1O_2$).[34] The fluorescence spectra of DCFH were recorded in the absence and in the presence of different nanoprobes under light illumination. As shown in Figure S6A and S6C, after exposure to white light for 70 s, DCFH showed very limited fluorescence enhancement in the presence of BSA@DTF NPs (1 μM) than that of DCFH alone. The ROS produced by BSA@DTF NPs was even fewer than that produced by DTF (Figure S6B) at the same concentration, suggesting that encapsulation by BSA indeed lower the ROS production of DTF molecules. In contrast, DSPE-PEG@DTF NPs and F127@DTF NPs (Figure S6D and S6E) induced obvious fluorescence enhancement of DCFH after being illuminated, reaching around 58 and 99 folds as that produced by BSA@
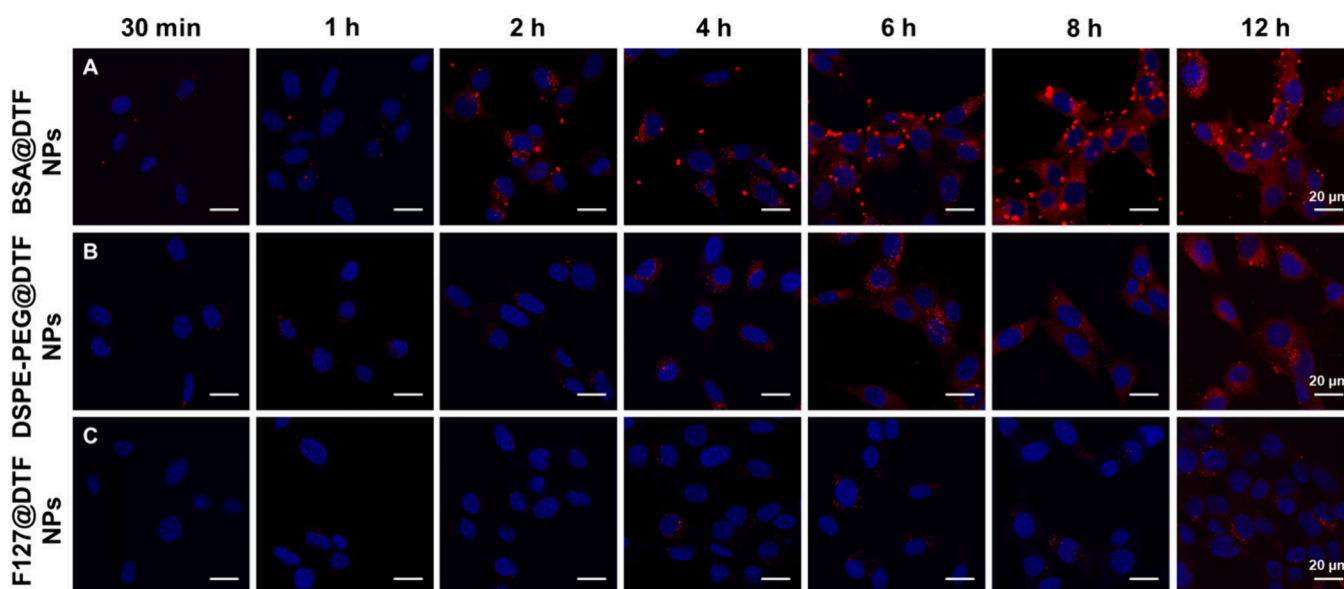
Figure 3. Confocal Images of HT-22 cells incubated with BSA@DTF NPs, DSPE-PEG@DTF NPs, and F127@DTF NPs for different periods of time as stated. The nuclei were stained with Hoechst 33342 (1 μg/mL, 20 min) showing blue fluorescence. All of the three nanoprobes share the same concentration at 15 μM for incubation. All the images share scale bar of 20 μm.

DTF NPs. The fluorescence intensity of DCFH in the presence of BSA@DTF NPs, DSPE-PEG@DTF NPs, and F127@DTF NPs at different time points was summarized in Figure 2A, from which the ROS generation efficiency of BSA@DTF NPs was calculated to be only 2.4% of that produced by F127@DTF NPs.

The $^1O_2$ generation ability of these nanoprobes was subsequently determined by measuring the absorption of 9,10-anthracenediyl-bis(methylene)dimalonic acid (ABDA) after light irradiation.[33] ABDA decomposed in the presence of $^1O_2$ with a declined absorption, which is quantitively related to the amount of $^1O_2$. As shown in Figure S7A and S7C, BSA@DTF NPs (1 μM) induced very limited ABDA decomposition after the white light illumination for 300 s, which is similar as that of ABDA alone and even less than that produced by DTF as shown in Figure S7B. In comparison, Figure S7E shows that in the presence of F127@DTF NPs at the same concentration, around 38% of ABDA decomposed after white light illumination for 300 s. DSPE-PEG@DTF NPs only induced a very small portion of ABDA decomposed as indicated in Figure S7D. The decomposition rate of ABDA ($\ln(A_0/A)$ vs time) was plotted and calculated to be 0.125, 0.032, and only 0.013 for F127@DTF, DSPE-PEG@DTF, and BSA@DTF NPs, respectively, as shown in Figure 2B.

The photothermal effects of the three nanoprobes were further evaluated by measuring the changes of temperature of the nanoprobes solution. As shown in Figure S8, under white light illumination at the power density of 30, 45, and 60 mW/cm², all of the three nanoprobes showed very minor temperature changes after illumination for 8 min, neither at the concentration of 1 nor 15 μM. The results indicated that none of the three nanoprobes have adequate photothermal effect to induce cell damage, which is actually favorable for fluorescence imaging. Figure 2D actually makes a comparison of the fluorescence intensity, ROS generation, and photothermal conversion efficiency of BSA@DTF NPs, DSPE-PEG@DTF NPs, and F127@DTF NPs. Collectively, these results revealed that the photophysical and photochemical

properties of AIEgens could be further adjusted through simple matrices optimization, even after synthesis of certain chemical structures. Particularly in this work, BSA@DTF NPs were the most suitable one for live cell imaging due to the best photoluminescent emission and neglected ROS and heat production.

In Vitro Fluorescent Imaging by the Three Nanoprobes Using HT-22 Cells

To further explore the advantages of BSA@DTF NPs over the other two nanoprobes in the fluorescent bioimaging in the CNS, the mouse hippocampal neuronal cell line HT-22, an important cell line for studying neurodegenerative diseases and testing potential neuronal therapies, was employed as the in vitro model in this work. The cellular toxicity of different nanoprobes was first evaluated by incubation with HT-22 cells for 12 h followed by CCK-8 assay, and the results were summarized and shown in Figure S9. In the following in vitro experiment, all of the nanoprobes were used with the same concentration of 15 μM according to the DTF content. First, to investigate the cellular uptake behaviors of BSA@DTF NPs, DSPE-PEG@DTF NPs, and F127@DTF NPs, they were incubated with HT-22 cells for different periods of time, from 30 min up to 12 h. The cellular uptake was assessed by confocal laser scanning microscopy (CLSM) with cell nuclei localized by blue emissive Hoechst 33342. As shown in Figure 3, BSA@DTF NPs enters HT-22 cells very quickly even after 30 min incubation, while DSPE-PEG@DTF NPs did not exhibit obvious fluorescence inside cells until 4 h incubation. The integrals of red fluorescence in each figure can be calculated with the assistance of ImageJ software; hence, the mass ratios of DTF could be determined after correcting the fluorescence integrals by the relative brightness of each nanoprobes. According to the calculated results, after coincubation for 2 h, only around 5% and 2.5% of DSPE-PEG@DTF NPs and F127@DTF NPs were uptaken by HT-22 cells, compared with that of BSA@DTF NPs. After 6 h of coincubation, the ratio of BSA@DTF NPs and DSPE-PEG@DTF NPs uptaken by HT-22 reached 2:1. As for F127@DTF
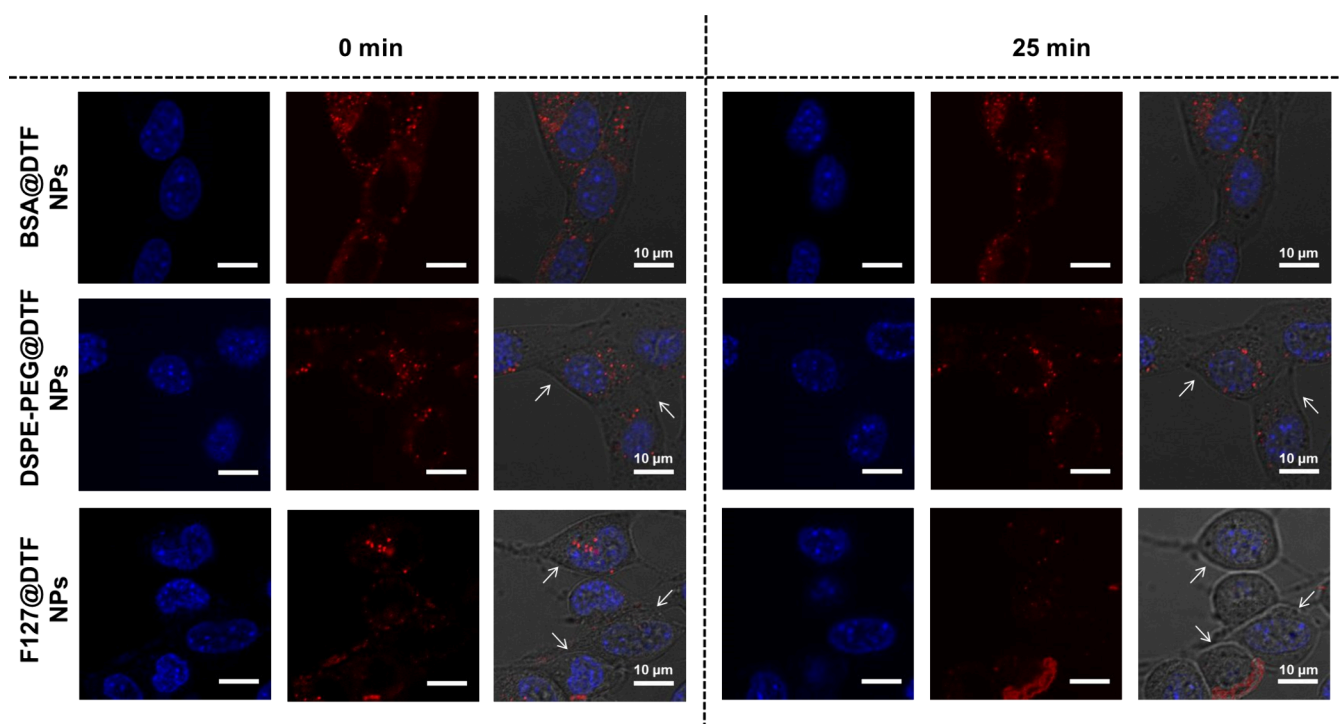
Figure 4. Confocal Images of HT-22 cells taken at time points of 0 and 25 min after exposure to 488 nm laser illumination. HT-22 cells are first incubated with BSA@DTF NPs, DSPE-PEG@DTF NPs, and F127@DTF NPs for 24 h and then their nuclei were stained by Hoechst 33342.
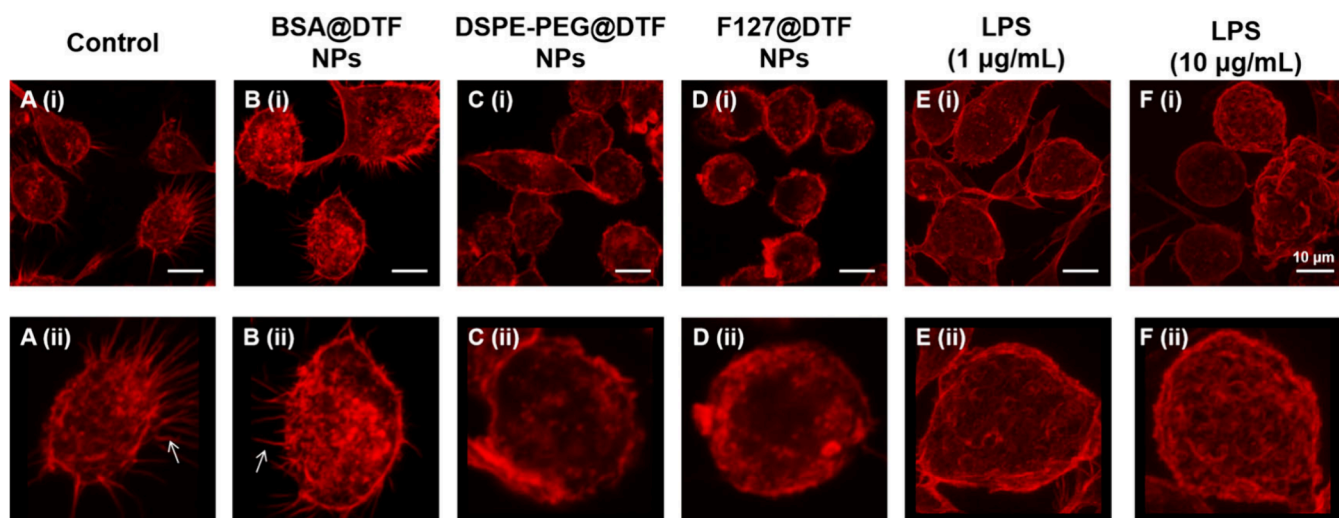

Figure 5. CLSM images of actin filaments in BV-2 cells incubated with BSA@DTF NPs, DSPE-PEG@DTF NPs, and F127@DTF NPs for 24 h, respectively. Actin filaments were stained by a red-emissive commercialized dye ActinRed 555 after the fixation of BV-2 cells with 4% paraformaldehyde.

NPs, it took around 12 h to exhibit obvious red fluorescence inside cells. After 12 h coincubation, though the same amount of DSPE-PEG@DTF NPs and BSA@DTF NPs were taken up by HT-22 cells, the former ones look much dimmer than the latter one. Collectively, the results demonstrated that BSA@DTF NPs enter the HT-22 cell much more quickly. Together with its better emissive brightness, it is a superior reagent for fluorescent bioimaging over the other two nanoprobes.

Subsequently, HT-22 cells were first incubated with BSA@DTF NPs for 24h, DSPE-PEG@DTF NPs, and F127@DTF NPs, respectively, and then illuminated by the 488 nm laser equipped on the CLSM. As shown in Figure 4 and Figure S10, HT-22 cells treated with F127@DTF NPs become rounded in

shape, suggesting a deterioration in their healthy situation. In comparison, BSA@DTF NPs did not exert much of an effect on the morphology of HT-22 cells. It is noteworthy that the number of BSA@DTF NPs taken up by HT-22 was much greater than that of F127@DTF NPs, which further suggests that BSA@DTF NPs are much less toxic than F127@DTF NPs. The intracellular ROS generation was indicated by the light-up fluorescence emitted by DCFH-DA probe, as shown in Figure S11, revealing that there are significant ROS generation in HT-22 cells treated with both DSPE-PEG@DTF NPs and F127@DTF NPs. In contrast, HT-22 cells coincubated with BSA@DTF NPs remain emissive under the same conditions.

BV-2 Cytoskeleton Morphology Changes after Incubation with Three Nanoprobes

Microglia are resident immune cells in the brain, which account for about 10−15% of cells in the brain and spinal cord. Microglia keep scanning the environment for danger signals and play both protective and detrimental functions by taking different phenotypes under certain circumstances. Microglia could polarize into M1 pro-inflammatory phenotype from resting phenotype (M0) in response to the inflammatory environmental stimuli. M1 microglia, which are also termed as classical activation state, are associated with further production of pro-inflammatory cytokines such as interleukin-1 β (IL-1 β), nitric oxide (NO), reactive oxygen species (ROS), etc. BV-2 cells are semiadherent cells with a range of heterogeneous appearance. It has been reported that resting microglia (M0) are activated by lipopolysaccharide (LPS) to M1 microglia, and experience a morphological transit from a ramified shape to an ameboid shape.[35,36] However, there are more frequent debates on the cell morphology of different phenotypes.[37]

In this part, the morphology changes of BV-2 cells before and after incubation with different nanoprobes, including BSA@DTF NPs, DSPE-PEG@DTF NPs, and F127@DTF NPs, were studied by staining their cytoskeleton. Specifically, BV-2 cells were first incubated with the three nanoprobes, and their actin filaments were stained by a commercialized dye ActinRed 555. Though BV-2 cells without any treatment show a range of morphology including normal shape, elongated, and oval cell shape, they are all characterized with one feature of many small protrusions on the outer parts of their cytoskeleton, particularly in the top cross sections of each cell, which are recorded clearly in CLSM images in Figure 5A. However, after incubated with DSPE-PEG@DTF NPs or F127@DTF NPs, most of BV-2 cells lost their small protrusions and some of the them become rounded in shape. In contrast, BV-2 cells incubated with BSA@DTF NPs did not show obvious changes in the morphology of their actin filaments. To figure out the reasons for the disappearance of the small protrusions on BV-2 cells treated with DSPE-PEG@DTF NPs and F127@DTF NPs, BV-2 cells were treated with LPS, which is a classic inducer of M1 microglia, and their actin filaments were also stained and observed by CLSM. Interestingly, BV-2 cells showed much less protrusion on their cell membrane after being treated with 1 μg/mL of LPS. Moreover, this phenomenon became much more obvious after treatment with 10 μg/mL of LPS, showing a concentration-dependent trend. The results indicated that to sustain normal cytoskeleton morphology of BV-2 cells, it is important to minimize the ROS generation of the bioimaging reagents, particularly for those with long-wavelength fluorescence emission. Collectively, BSA@DTF NPs showed much less side effects on sensitive cells such as microglia, which is important for fluorescent imaging in the CNS.

CONCLUSIONS

In conclusion, this study investigated the effect of encapsulation on the photoluminescent properties, ROS generation, and photothermal conversion rate of AIEgen using various matrices including BSA, DSPE-PEG$_{2000}$, and F127. Interesting, compared with F127@DTF NPs, BSA@DTF NPs showed 1.3 folds of brightness but only produced around 2.4% of ROS. The potential of BSA@DTF NPs for the live cell imaging particularly for CNS was evaluated using HT-22 cell. The

results demonstrated better cellular uptake, negligible intra-cellular ROS, and phototoxicity even after a continuous illumination for 25 min. It is noteworthy that the small protrusions outside the cytoskeleton of BV-2 cells vanished after incubation with DSPE-PEG@DTF NPs or F127@DTF NPs, similar to those treated with LPS. In contrast, BSA@DTF NPs preserved the normal cytoskeleton morphology of BV-2 cells, akin to untreated control group. This work represents a successful but easy-to-operate process to suppress the ROS generation of red-emissive AIEgens. It underscores the critical importance of minimizing the ROS generation of the fluorescent probes, particularly for long-term imaging applications involving CNS cells.

■ ASSOCIATED CONTENT

ⓢ Supporting Information

The Supporting Information is available free of charge at https://pubs.acs.org/doi/10.1021/cbmi.4c00061.

> Additional experimental details, materials, reagents, HRMS(ESI-MS) and NMR spectra, size, and morphology of nanoprobes, and supporting figures (PDF)

■ AUTHOR INFORMATION

Corresponding Authors

Xiaoqiong Li − *Institute of Engineering Medicine, School of Medical Technology, Beijing Key Laboratory for Separation and Analysis in Biomedicine and Pharmaceuticals, Beijing Institute of Technology, Beijing 100081, P. R. China*; Email: aeople@126.com

Wenbo Wu − *Department of Chemistry, Institute of Molecular Aggregation Science, Tianjin University, Tianjin 300072, P. R. China*; ⓞ orcid.org/0000-0002-6794-217X; Email: wuwb@tju.edu.cn

Ruoyu Zhang − *Institute of Engineering Medicine, School of Medical Technology, Beijing Key Laboratory for Separation and Analysis in Biomedicine and Pharmaceuticals, Beijing Institute of Technology, Beijing 100081, P. R. China*; ⓞ orcid.org/0000-0002-4086-9566; Email: ryzhqd@hotmail.com

Yulin Deng − *Institute of Engineering Medicine, School of Medical Technology, Beijing Key Laboratory for Separation and Analysis in Biomedicine and Pharmaceuticals, Beijing Institute of Technology, Beijing 100081, P. R. China*; ⓞ orcid.org/0000-0002-0720-4052; Email: deng@bit.edu.cn

Authors

Xiaotong Chen − *Institute of Engineering Medicine, School of Medical Technology, Beijing Key Laboratory for Separation and Analysis in Biomedicine and Pharmaceuticals, Beijing Institute of Technology, Beijing 100081, P. R. China*

Yajing Jiang − *Department of Chemistry, Institute of Molecular Aggregation Science, Tianjin University, Tianjin 300072, P. R. China*

Jiaxin Liu − *Department of Chemistry, Institute of Molecular Aggregation Science, Tianjin University, Tianjin 300072, P. R. China*

Yu Tian − *Department of Chemistry, Institute of Molecular Aggregation Science, Tianjin University, Tianjin 300072, P. R. China*

Yifan Deng − *Institute of Engineering Medicine, School of Medical Technology, Beijing Key Laboratory for Separation*

and Analysis in Biomedicine and Pharmaceuticals, Beijing Institute of Technology, Beijing 100081, P. R. China

Complete contact information is available at:
https://pubs.acs.org/10.1021/cbmi.4c00061

Notes

The authors declare no competing financial interest.

REFERENCES

(1) Wei, W.; Qiu, Z. Diagnostics and theranostics of central nervous system diseases based on aggregation-induced emission luminogens. *Biosens. Bioelectron.* **2022**, *217*, 114670.

(2) Misgeld, T.; Kerschensteiner, M. In vivo imaging of the diseased nervous system. *Nat. Rev. Neurosci.* **2006**, *7*, 449−463.

(3) Qi, Y.-L.; Wang, H.-R.; Chen, L.-L.; Guo, L.; Cao, Y.-Y.; Yang, Y.-S.; Duan, Y.-T.; Zhu, H.-L. Recent advances in reaction-based fluorescent probes for the detection of central nervous system-related pathologies in vivo. *Coord. Chem. Rev.* **2021**, *445*, 214068.

(4) Giepmans, B. N.; Adams, S. R.; Ellisman, M. H.; Tsien, R. Y. The fluorescent toolbox for assessing protein location and function. *Science* **2006**, *312*, 217−224.

(5) Nguyen, Q. T.; Tsien, R. Y. Fluorescence-guided surgery with live molecular navigation — a new cutting edge. *Nat. Rev. Cancer* **2013**, *13*, 653−662.

(6) Lee, M. H.; Kim, J. S.; Sessler, J. L. Small molecule-based ratiometric fluorescence probes for cations, anions, and biomolecules. *Chem. Soc. Rev.* **2015**, *44*, 4185−4191.

(7) Qi, Y.-L.; Wang, H.-R.; Chen, L.-L.; Duan, Y.-T.; Yang, S.-Y.; Zhu, H.-L. Recent advances in small-molecule fluorescent probes for studying ferroptosis. *Chem. Soc. Rev.* **2022**, *51*, 7752−7778.

(8) Li, H.; Kim, H.; Xu, F.; Han, J.; Yao, Q.; Wang, J.; Pu, K.; Peng, X.; Yoon, J. Activity-based NIR fluorescent probes based on the versatile hemicyanine scaffold: design strategy, biomedical applications, and outlook. *Chem. Soc. Rev.* **2022**, *51*, 1795−1835.

(9) Li, B.; Zhao, M.; Zhang, F. Rational Design of Near-Infrared-II Organic Molecular Dyes for Bioimaging and Biosensing. *ACS Mater. Lett.* **2020**, *2*, 905−917.

(10) Wu, J.; Shi, Z.; Zhu, L.; Li, J.; Han, X.; Xu, M.; Hao, S.; Fan, Y.; Shao, T.; Bai, H.; Peng, B.; Hu, W.; Liu, X.; Yao, C.; Li, L.; Huang, W. The Design and Bioimaging Applications of NIR Fluorescent Organic Dyes with High Brightness. *Adv. Opt. Mater.* **2022**, *10* (8), 2102514.

(11) Xu, W.; Wang, D.; Tang, B. Z. NIR-II AIEgens: a win-win integration towards bioapplications. *Angew. Chem., Int. Ed.* **2021**, *60*, 7476−7487.

(12) Liu, S.; Li, Y.; Kwok, R. T. K.; Lam, J. W. Y.; Tang, B. Z. Structural and process controls of AIEgens for NIR-II theranostics. *Chem. Sci.* **2021**, *12*, 3427−3436.

(13) Lei, Z.; Zhang, F. Molecular engineering of NIR-II fluorophores for improved biomedical detection. *Angew. Chem., Int. Ed.* **2021**, *60*, 16294−16308.

(14) Xu, S.; Duan, Y.; Liu, B. Precise Molecular Design for High-Performance Luminogens with Aggregation-Induced Emission. *Adv. Mater.* **2020**, *32*, No. e1903530.

(15) Yang, X.; Wang, X.; Zhang, X.; Zhang, J.; Lam, J. W. Y.; Sun, H.; Yang, J.; Liang, Y.; Tang, B. Z. Donor-Acceptor Modulating of Ionic AIE Photosensitizers for Enhanced ROS Generation and NIR-II Emission. *Adv. Mater.* **2024**, *36* (28), 2402182.

(16) Liang, M.; Liu, L.; Sun, Y.; Li, J.; Zhang, L. e.; Jiang, X.; Wu, W. Furan-modified thiadiazolo quinoxaline as an electron acceptor for constructing second near-infrared aggregation-induced emission fluorophores for beyond 1300 nm fluorescence/photoacoustic imaging and photothermal therapy. *Aggregate* **2024**, *5*, No. e458.

(17) He, X.; Luo, Y.; Li, Y.; Pan, Y.; Kwok, R. T. K.; He, L.; Duan, X.; Zhang, P.; Wu, A.; Tang, B. Z.; Li, J. D-type neuropeptide decorated AIEgen/RENP hybrid nanoprobes with light-driven ROS generation ability for NIR-II fluorescence imaging-guided through-skull photodynamic therapy of gliomas. *Aggregate* **2024**, *5*, No. e396.

(18) Forman, H. J.; Zhang, H. Targeting oxidative stress in disease: promise and limitations of antioxidant therapy. *Nat. Rev. Drug Discovery* **2021**, *20*, 689−709.

(19) Rekatsina, M.; Paladini, A.; Piroli, A.; Zis, P.; Pergolizzi, J. V.; Varrassi, G. Pathophysiology and Therapeutic Perspectives of Oxidative Stress and Neurodegenerative Diseases: A Narrative Review. *Adv. Ther.* **2020**, *37*, 113−139.

(20) Feng, W.; Han, X.; Hu, H.; Chang, M.; Ding, L.; Xiang, H.; Chen, Y.; Li, Y. 2D vanadium carbide MXenzyme to alleviate ROS-mediated inflammatory and neurodegenerative diseases. *Nat. Commun.* **2021**, *12*, 2203.

(21) Janjua, T. I.; Cao, Y.; Yu, C.; Popat, A. Clinical translation of silica nanoparticles. *Nat. Rev. Mater.* **2021**, *6*, 1072−1074.

(22) Li, K.; Qin, W.; Ding, D.; Tomczak, N.; Geng, J.; Liu, R.; Liu, J.; Zhang, X.; Liu, H.; Liu, B.; Tang, B. Z. Photostable fluorescent organic dots with aggregation-induced emission (AIE dots) for noninvasive long-term cell tracing. *Sci. Rep.* **2013**, *3*, 1150.

(23) Elsabahy, M.; Wooley, K. L. Design of polymeric nanoparticles for biomedical delivery applications. *Chem. Soc. Rev.* **2012**, *41*, 2545−2561.

(24) Tang, Z.; He, C.; Tian, H.; Ding, J.; Hsiao, B. S.; Chu, B.; Chen, X. Polymeric nanostructured materials for biomedical applications. *Prog. Polym. Sci.* **2016**, *60*, 86−128.

(25) Antaris, A. L.; Chen, H.; Diao, S.; Ma, Z.; Zhang, Z.; Zhu, S.; Wang, J.; Lozano, A. X.; Fan, Q.; Chew, L.; Zhu, M.; Cheng, K.; Hong, X.; Dai, H.; Cheng, Z. A high quantum yield molecule-protein complex fluorophore for near-infrared II imaging. *Nat. Commun.* **2017**, *8*, 15269.

(26) Li, Y.; Zhang, D.; Yu, Y.; Zhang, L.; Li, L.; Shi, L.; Feng, G.; Tang, B. Z. A Cascade Strategy Boosting Hydroxyl Radical Generation with Aggregation-Induced Emission Photosensitizers-Albumin Complex for Photodynamic Therapy. *ACS Nano* **2023**, *17*, 16993−17003.

(27) Geng, J.; Goh, C. C.; Tomczak, N.; Liu, J.; Liu, R.; Ma, L.; Ng, L. G.; Gurzadyan, G. G.; Liu, B. Micelle/Silica Co-protected Conjugated Polymer Nanoparticles for Two-Photon Excited Brain Vascular Imaging. *Chem. Mater.* **2014**, *26*, 1874−1880.

(28) Wu, W.; Xu, S.; Qi, G.; Zhu, H.; Hu, F.; Liu, Z.; Zhang, D.; Liu, B. A Cross-linked Conjugated Polymer Photosensitizer Enables Efficient Sunlight-Induced Photooxidation. *Angew. Chem., Int. Ed.* **2019**, *58*, 3062−3066.

(29) Han, X.; Bai, Q.; Yao, L.; Liu, H.; Gao, Y.; Li, J.; Liu, L.; Liu, Y.; Li, X.; Lu, P.; Yang, B. Highly Efficient Solid-State Near-Infrared Emitting Material Based on Triphenylamine and Diphenylfumaronitrile with an EQE of 2.58% in Nondoped Organic Light-Emitting Diode. *Adv. Funct. Mater.* **2015**, *25*, 7521−7529.

(30) Wu, W.; Mao, D.; Hu, F.; Xu, S.; Chen, C.; Zhang, C. J.; Cheng, X.; Yuan, Y.; Ding, D.; Kong, D.; Liu, B. A Highly Efficient and Photostable Photosensitizer with Near-Infrared Aggregation-Induced Emission for Image-Guided Photodynamic Anticancer Therapy. *Adv. Mater.* **2017**, *29* (33), 1700548.

(31) Park, J.; Lee, J.; Choi, C. Mitochondrial Network Determines Intracellular ROS Dynamics and Sensitivity to Oxidative Stress through Switching Inter-Mitochondrial Messengers. *PLoS One* **2011**, *6*, e23211.

(32) Bourré, L.; Thibaut, S.; Briffaud, A.; Rousset, N.; Eléouet, S.; Lajat, Y.; Patrice, T. Indirect detection of photosensitizer ex vivo. *J. Photochem. Photobiol., B* **2002**, *67*, 23−31.

(33) Entradas, T.; Waldron, S.; Volk, M. The detection sensitivity of commonly used singlet oxygen probes in aqueous environments. *J. Photochem. Photobiol., B* **2020**, *204*, 111787.

(34) Wang, Y.; Liao, J.; Lyu, Y.; Guo, Q.; Zhu, Z.; Wu, X.; Yu, J.; Wang, Q.; Zhu, W. H. An AIE Photosensitizer with Simultaneous Type I and Type II ROS Generation: Efficient Bacterial Elimination and Hypoxic Tumor Ablation. *Adv. Funct. Mater.* **2023**, *33* DOI: 10.1002/adfm.202301692.

(35) Kim, C.; Cho, E.-D.; Kim, H.-K.; You, S.; Lee, H.-J.; Hwang, D.; Lee, S.-J. β1-integrin-dependent migration of microglia in response to neuron-released α-synuclein. *Exp. Mol. Med.* **2014**, *46*, No. e91.

(36) Kim, C.; Ho, D. H.; Suk, J. E.; You, S.; Michael, S.; Kang, J.; Joong Lee, S.; Masliah, E.; Hwang, D.; Lee, H. J.; Lee, S. J. Neuron-released oligomeric alpha-synuclein is an endogenous agonist of TLR2 for paracrine activation of microglia. *Nat. Commun.* **2013**, *4*, 1562.

(37) Tang, Y.; Le, W. Differential Roles of M1 and M2Microglia in Neurodegenerative Diseases. *Mol. Neurobiol.* **2016**, *53*, 1181−1194.